

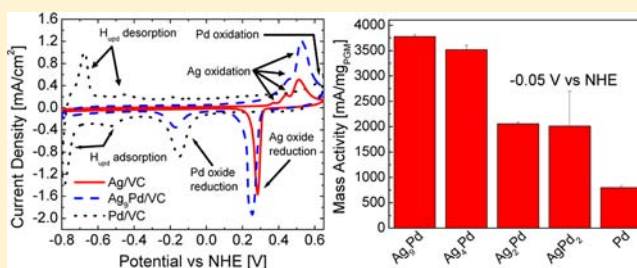
Atomic Ensemble and Electronic Effects in Ag-Rich AgPd Nanoalloy Catalysts for Oxygen Reduction in Alkaline Media

Daniel A. Slanac,[†] William G. Hardin,^{||} Keith P. Johnston,^{*,†,§,||} and Keith J. Stevenson^{*,‡,§,||}

[†]Department of Chemical Engineering, [‡]Department of Chemistry and Biochemistry, [§]Center for Electrochemistry, and ^{||}The Texas Materials Institute, The University of Texas at Austin, Austin, Texas 78712, United States

Supporting Information

ABSTRACT: The ability to design and characterize uniform, bimetallic alloy nanoparticles, where the less active metal enhances the activity of the more active metal, would be of broad interest in catalysis. Herein, we demonstrate that simultaneous reduction of Ag and Pd precursors provides uniform, Ag-rich AgPd alloy nanoparticles (~5 nm) with high activities for the oxygen reduction reaction (ORR) in alkaline media. The particles are crystalline and uniformly alloyed, as shown by X-ray diffraction and probe corrected scanning transmission electron microscopy. The ORR mass activity per total metal was 60% higher for the AgPd₂ alloy relative to pure Pd. The mass activities were 2.7 and 3.2 times higher for Ag₉Pd (340 mA/mg_{metal}) and Ag₄Pd (598 mA/mg_{metal}), respectively, than those expected for a linear combination of mass activities of Ag (60 mA/mg_{Ag}) and Pd (799 mA/mg_{Pd}) particles, based on rotating disk voltammetry. Moreover, these synergy factors reached 5-fold on a Pd mass basis. For silver-rich alloys (Ag_{≥4}Pd), the particle surface is shown to contain single Pd atoms surrounded by Ag from cyclic voltammetry and CO stripping measurements. This morphology is favorable for the high activity through a combination of modified electronic structure, as shown by XPS, and ensemble effects, which facilitate the steps of oxygen bond breaking and desorption for the ORR. This concept of tuning the heteroatomic interactions on the surface of small nanoparticles with low concentrations of precious metals for high synergy in catalytic activity may be expected to be applicable to a wide variety of nanoalloys.



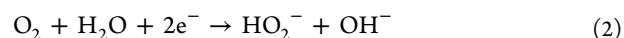
INTRODUCTION

Bimetallic catalysts have garnered considerable interest because they exhibit distinctly different and often superior activity for many chemical transformations as compared to pure monometallic systems as determined via DFT calculations^{1–3} and experimental studies.^{4–7} The enhanced performance of bimetallic catalysts may be rationalized by a combination of ligand, geometric, and/or ensemble effects.^{1,8,9} Ligand effects, charge transfer between nearest neighbor atoms, and geometric effects, primarily compressive or tensile strain, generally influence the strength of interactions of reactants, intermediates, and products. Ensemble effects result when more than one reactive site, composed of different metal atoms or clusters of atoms, catalyzes distinct steps in a reaction mechanism. Whereas ensemble effects are well-known in gas-phase heterogeneous catalysis,^{8–11} they have received limited attention in electrocatalysis.^{12–14}

To understand how to employ ligand, geometric, and/or ensemble effects to achieve high catalyst activity, we have chosen the oxygen reduction reaction (ORR) as a model system. The kinetic limitations in the ORR are a major concern for both metal–air batteries and low-temperature fuel cells.^{15–21} In base, the two main pathways for the ORR are the direct four-electron transfer:



and a 2 by 2 electron (stepwise) pathway:



which goes through a hydroperoxide intermediate (HO₂⁻). The combination of reactions 2 and 3 yield reaction 1, although the kinetics of reaction 3 can be limiting. Furthermore, the HO₂⁻ intermediate can undergo disproportionation according to:



Bimetallic catalysts may be designed to efficiently target this set of reaction pathways to achieve high synergy among the various metal atoms.

For core–shell catalysts, the combination of ligand and geometric effects provides exceptionally high ORR activity.^{6,22–24} Here, an electronic shift and geometric strain in the shell, due to the underlying core, favorably modify the binding energies of reaction intermediates, particularly in the direct four-electron transfer. For example, a Pt or Pd monolayer shell deposited on a transition metal core produced activities per mass of noble metal up to 8× times relative to the pure noble metal.^{22,25} However, when the diameter of a core–shell catalyst

Received: April 14, 2012

Published: May 17, 2012

becomes <5 nm, a monolayer shell would comprise greater than >30% of the total atoms in the particle. In contrast, even lower precious metal concentrations are possible for homogeneous bimetallic nanoalloys. Furthermore, the large number of contacts between dissimilar metals promotes ensemble effects, as well as ligand effects. However, for ORR nanoparticle catalysts, precious noble metal contents are typically >50% due to challenges in synthesis.^{4,5,7,26}

To design an active nanoalloy catalyst with a low content of a highly active precious noble metal and a second less active metal, it would be desirable to achieve strong ligand and ensemble effects. For the ORR in alkaline media, less-expensive precious metals such as Ag exhibit good ORR activity, especially for HO₂⁻ disproportionation,²⁷ and are more stable^{20,21,28,29} than in acid, enabling them to be used in nanoalloys with Pd.^{30–34} Because the cost ratio of Pd:Ag is ~22:1, it would be economically desirable to utilize both metals in a bifunctional manner to raise activity and improve stability. However, for a case where the Pd level was only 20 mol % (Ag₄Pd), the activity was not above the level expected from a linear combination of activities of the pure components.³⁰ To design structure and atomic surface arrangements of bimetallic nanoalloys for ligand and ensemble effects, improved synthetic methods are needed for controlling composition, morphology, and architecture (e.g., random-alloy vs core–shell). Alloy nanoparticles have been presynthesized in the presence of stabilizing ligands by arrested growth precipitation^{13,35–37} or in microemulsions^{38,39} and then later adsorbed onto the catalyst support. Dendrimer encapsulated nanoparticles have been synthesized with controlled alloy formation, for example, with Pd compositions just below 50 mol % (Pd₃₆Cu₆₄).⁴⁰ Recently, large 40 nm Au₄Pd alloy nanoparticles have been shown to exhibit higher activity than their core–shell morphologies, as a result of strong ensemble effects.¹³ However, we are not aware of small nanoalloys (<5 nm) with low amounts of a precious metal in the surface, where electronic and ensemble effects produce high activities.

Herein, we synthesize uniform bimetallic nanoalloy catalyst (~5 nm), with as little as ~10 mol % Pd (Ag₉Pd), to achieve high activity for the oxygen reduction reaction (ORR) in alkaline media. To control the distribution of the Pd and Ag on the surface, the nanoalloys with Ag compositions from ~40% to ~90% were synthesized by coreduction of Ag and Pd carboxylic acid complexes precursors at similar rates⁴¹ in the presence of stabilizing ligands. The nanoparticles were found to be uniformly alloyed, displaying a single alloy composition among the particles, as shown by a combination of X-ray diffraction (XRD), cyclic voltammetry (CV), and X-ray photoelectron spectroscopy (XPS). Furthermore, detailed probe-corrected scanning transmission electron microscopy (pcSTEM) analysis is presented for the Ag₉Pd catalyst. As a consequence of the low overall Pd content for Ag_{2–4}Pd and the uniformity of the alloying, the Pd atoms on the surface were surrounded primarily by Ag atoms, as characterized by the surface sensitive electrochemical techniques, cyclic voltammetry, and CO stripping measurements. Our hypothesis is that nearly all of the contacts of the more active metal Pd will be with Ag for Ag_{2–4}Pd, and these unlike interactions will enhance catalyst activity through electronic interactions (ligand effect), as was observed by the binding energy shift from XPS, and the cooperation of each metal toward various ORR reaction steps (ensemble effect). We found that the activities for Ag₉Pd and Ag₄Pd were up to 2.7- and 3.2-fold above the value expected

from the pure metals, a large nonlinear enhancement for ORR. Furthermore, the total metal mass activity for the AgPd₂ catalyst is 60% higher than for pure Pd, suggesting high synergy is also present for alloys with higher Pd loading. These results are compared to those of pure Ag and pure Pd nanoparticles of similar size on carbon. Furthermore, it appears that the sintering of pure Ag particles during calcination is mitigated by the addition of a small amount (10 mol %) of Pd in the alloy, again illustrating cooperative effects for the uniform alloy. Ultimately, the ability to disperse small amounts of a highly active precious metal within a less active metal on a nanoalloy surface is a general strategy that may offer significant benefit for scientific and practical advancement in catalysis.

EXPERIMENTAL SECTION

All chemicals were used as received. Silver nitrate, palladium acetate, tripropylamine, anhydrous ethanol, tetradecanoic acid, and 5 wt % nafion solution in lower alcohols were purchased from Sigma-Aldrich. Hexane (99.9%) and potassium hydroxide were obtained from Fisher Scientific, and ethanol (Absolute 200 proof) was from Aaper alcohol. Millipore high purity water (18 MΩ) was used. Vulcan XC72 (VC) carbon was obtained from Cabot Corp. Oxygen (research grade, 99.999% purity), argon (research grade, 99.999% purity), and CO (99.9%) were obtained from Praxair. Commercial 20% Pd/VC was obtained from ETEK.

Catalyst Synthesis. Particle Synthesis. Pd-tetradecanoate (Pd-TDOA) and Ag-tetradecanoate (Ag-TDOA) precursor powders were synthesized from palladium acetate and silver nitrate salts in organic and aqueous ligand substitution reactions, respectively, as reported previously.^{41,42}

The total concentration of metal atoms in the syntheses of both alloy and pure component nanoparticles was controlled to 0.71 M. The desired molar ratio of Ag-TDOA or Pd-TDOA was added to a 10 mL round-bottom reaction flask with 1.414 mL of tripropylamine.⁴¹ The solution was slowly heated under argon to 100 °C while being vigorously stirred. The solution was left at 100 °C for 1 h, and then cooled to room temperature. Acetone was then added in excess, and the solution was centrifuged for 5 min at 2000 rpm. This washing step was done three times, discarding the supernatant and replacing it with fresh acetone after each wash. Finally, the particles were added to hexane and centrifuged for 2 min at 10 000 rpm to narrow the size distribution. The hexane was evaporated, and the yield of nanoparticles was quantified. Finally, the particles were suspended in *n*-hexane to a 10 mg/mL concentration, which was black in color.

Adsorption of Particles onto Carbon Support. Aside from the commercial Pd/VC, all catalyst powders were prepared via adsorption of presynthesized nanoparticles onto Vulcan carbon. Vulcan XC72 carbon was mixed with an appropriate volume of nanoparticle solution (10 mg/mL in hexane) to achieve a loading of 20 wt % metal (assuming 100% adsorption of the particles). The carbon and nanoparticle solution was stirred for 1 h. The mixture was vacuum filtered. The color of the filtrate came out clear, indicating essentially complete adsorption of the particles on the carbon. The catalyst powder was calcined at 450 °C under forming gas, in a quartz tube furnace. The furnace was held at room temperature for 30 min, ramped to the desired temperature over 2 h, and held at 450 °C for 2 h. However, for the 10 nm Ag/VC catalysts, the same calcination procedure was used but with a maximum temperature of 210 °C. The calcined catalyst powder was then washed with 100 mL of EtOH, dried at 60 °C for 20 min, and stored under ambient conditions.

Electron Microscopy. Transmission Electron Microscopy (TEM). Low-mag TEM was conducted on an FEI Tecnai 20 BioTwin microscope using an 80 kV accelerating voltage. The carbon supported catalysts were deposited from a dilute ethanol suspension onto a 200 mesh copper grid coated with lacey carbon (Electron Microscopy Sciences). Average particle sizes were calculated from measurements of ~100 particles using ImageJ.

Scanning Transmission Electron Microscopy (STEM). High-resolution probe corrected STEM (pcSTEM) imaging was performed on a JEOL JEM-ARM200F probe aberration corrected electron microscope, operated at 200 kV. The probe size used was of 0.08 nm with a current of 24 pA. The spherical aberration was reduced with a dodecapole corrector (CEOS). Calibration was done using standard Si[110] and Au nanoparticles to align the corrector with CESCOR software. Images were recorded in STEM mode by simultaneously collecting bright field and high angle annular dark field (HAADF) images from scans of 12 to 16 s with a probe size of 0.08 Å. To determine the extent of alloying in the Ag₉Pd particles, energy dispersive X-ray spectroscopic (EDS) line scans were performed on individual particles using a probe size of ~1.3 Å, a step size of 2 Å, and a dwell time of 5 s, while correcting for spatial drift.

X-ray Diffraction (XRD). Wide-angle X-ray diffraction was performed on a film of carbon supported catalyst powders on a quartz slide with a Bruker Nokius instrument using Cu K α radiation (1.54 Å wavelength). Samples were scanned from 10° to 90° in 0.02° increments with a dwell time of 10 s. The average nanoparticle size was estimated from the Scherrer equation in JADE software (Molecular Diffraction Inc.). Background correction, fitting, and deconvolution were done using JADE software. The *d*-spacing is calculated from $d_{hkl} = \lambda / (2 \sin \theta)$, while the lattice parameter is calculated according to $a = d_{hkl} \cdot (h^2 + k^2 + l^2)^{1/2}$, where *h*, *k*, and *l* are the Miller indices for the crystal plane, λ is the X-ray wavelength, and θ is the angle of the peak for the crystal plane reflection.

X-ray Photoelectron Spectroscopy (XPS). XPS was acquired using a Kratos AXIS Ultra DLD spectrometer equipped with a monochromatic Al X-ray source (Al α , 1.4866 keV). High-resolution elemental analysis was performed on the Pd 3d and Ag 3d regions with a 20 eV pass energy, a 0.1 eV step, and a 4 s dwell time. Charge compensation was not used as each sample was conductive. All absolute energies were calibrated relative to gold, silver, and graphite. The peak positions and areas are calculated using a standard Gaussian + Lorentzian fit with a Shirley background correction.

Thermogravimetric Analysis (TGA). Thermogravimetric analysis was made with a Mettler Toledo TGA/DSC 1 STARe system equipped with a gas controller (GC 200) and a recirculating stage cooling bath set at 22 °C (Julabo). A sample size of >2 mg of carbon supported catalysts after calcination was used for analysis. The gas flow rate during the analysis was controlled at 60 mL_{air}/min. The catalysts were initially held at 110 °C for 10 min to drive off any solvents. Next, the catalysts were heated directly to 900 at 20 °C/min. The final mass remaining after the analysis was used to calculate the total metal loading (wt %).

Electrochemical Characterization. Catalyst inks were prepared by adding 1 mL of a 0.05 wt % Nafion solution to 1 mg of catalyst powder and sonicating for 30 min. Ten microliters of ink was drop cast onto a clean 5 mm (0.196 cm²) glassy carbon electrode and left to dry under a glass vial. The glassy carbon electrodes were cleaned prior to drop casting by sonication in a 1:1 DI water:ethanol solution. The electrode was then polished using 0.05 μ m alumina powder, sonicated in a fresh DI water:ethanol solution, and dried in ambient air. All electrochemical tests were performed on electrodes prepared by this method, such that the metal loading for all catalysts was 10 μ g/cm².

Electrochemical testing was performed on either a CH Instruments CHI832a or a Metrohm Autolab PGSTAT302N potentiostat, both equipped with high speed rotators from Pine Instruments. Each test was performed in a standard three-electrode cell, with a Hg/HgO (1 M KOH) reference electrode, a Pt wire counter electrode, and the catalyst ink film on glass carbon as the working electrode. All testing was done at room temperature in 0.1 M KOH. The solution was deaerated by bubbling argon for at least 10 min. The catalyst was electrochemically cycled from -0.9 to 0.25 V (Hg/HgO) at 20 mV/s for 10 cycles to clean the surface. Immediately following the cleaning procedure, an extended cyclic voltammogram (CV) from -0.9 to 0.55 V at 20 mV/S for two cycles was performed to identify the oxidation/reduction for both Ag and Pd. The total amount of charge to reduce the oxidized metal surface was used to estimate the surface composition of the catalyst. The oxidation of silver involves one

electron per silver atom ($\text{Ag}_2\text{O} + \text{H}_2\text{O} + 2e \rightarrow 2\text{Ag} + 2\text{OH}^-$ or $\text{AgOH} + e \rightarrow \text{Ag} + \text{OH}^-$),⁴³ while the reduction of Pd oxide requires two electrons ($\text{Pd}(\text{OH})_2 + 2e \rightarrow \text{Pd} + 2\text{OH}^-$).⁴⁴ The electrolyte was then saturated with oxygen by bubbling for a minimum of 10 min. ORR activity measurements were taken by rotating the electrode at 1600 rpm and performing a linear sweep from 0.2 to -0.6 V at 5 mV/s. Kinetic currents were used to evaluate mass activities and were taken at -0.05 V vs NHE from the polarization curves. The kinetic current was calculated according to the Koutecky-Levich equation: $1/i = (1/i_d) + (1/i_k)$. The number of electrons transferred, *n*, for the ORR was calculated on the basis of the diffusion-limited current according to the Levich equation: $i_d = 0.620nFAD^{2/3}\omega^{1/2}\nu^{-1/6}C$, where *F* is Faraday's constant (96 485 C/mol), *A* is electrode area (0.196 cm²), *D* is diffusion coefficient for dissolved oxygen (2×10^{-5} cm²/s), ω is scan rate (1600 rpm or 167.7 rad/s), ν is kinematic viscosity (0.01 cm²/s), and *C* is the saturated oxygen concentration in 0.1 M KOH at an oxygen partial pressure of 1 atm (1.2×10^{-6} mol/cm³).²¹

CO stripping was performed to determine the surface composition of the catalyst. The solution was saturated with CO by bubbling for 30 min. The potential of the electrode was held at -0.8 V (Hg/HgO) for 15 min. The solution was then purged with Ar while still holding the potential at -0.8 V (Hg/HgO) for 20 min. The potential was then cycled three times between -0.8 and 0.3 V (Hg/HgO).

RESULTS AND DISCUSSION

To realize the electronic and ensemble effects, the catalyst composition and morphology were controlled via thermolysis of organometallic precursors in the presence of capping ligands to arrest particle growth, as demonstrated for other alloy systems.^{35–37,45} Ag and Pd were separately complexed to tetradecanoic acid, which acted as a capping agent to arrest the growth of the particles after reduction by tripropylamine.⁴¹ The similar reduction rates of the complexes yielded small (~3–5 nm), relatively monodisperse sizes for the AgPd alloys and pure Ag nanoparticles determined via TEM and shown by micrographs for Ag₉Pd (3.2 ± 0.6 nm) and Ag (4.3 ± 0.7 nm) in Figures S1A,D and S2A,D, respectively. The alloy particles (for Ag₉Pd) after adsorption onto the carbon support and removal of the ligands at 450 °C in nitrogen remain small and uniformly dispersed on the carbon (5.3 nm, Figures 1A, S1B, and S1E), as is also seen for the commercial Pd particles (5.7 nm, Figure S1C,F). Similar sizes were obtained for the other AgPd alloy ratios in Table 1. With only 10 mol % Pd, the nanoalloy particles were resistant to sintering at 450 °C, whereas the pure Ag particles coalesced to 19 nm (Figure S2C,F). The Pd acts to effectively lower bulk atomic mobility and movement of the particles on the support during calcination, thereby strongly anchoring the particles and mitigating thermal sintering.⁴⁶ For a lower calcination temperature of 210 °C, the degree of sintering for pure Ag is mitigated, yielding a final particle size of 10 nm (Figure S2B). The alloy particles displayed an FCC crystal structure as shown by the characteristic {111}, {200}, {220}, {311}, and {222} reflections in their XRD spectrum (Figures 1B, S3). This structure is expected as both Pd and Ag are FCC crystalline materials. Scherrer analysis was performed on the {111} reflections to calculate crystallite sizes. The values span from ~4–8 nm as summarized in Table 1, consistent with the values measured via TEM. Probe-corrected STEM was performed on the Ag₉Pd catalyst, clearly showing the crystalline nature of the particle (Figure 1C). Electron diffraction reveals that the particle surface is dominated by {111} planes and contains twinning, common among Ag nanoparticles.⁴⁷

Uniform alloying among the particles was achieved by the simultaneous reduction of Ag and Pd at similar rates, as a

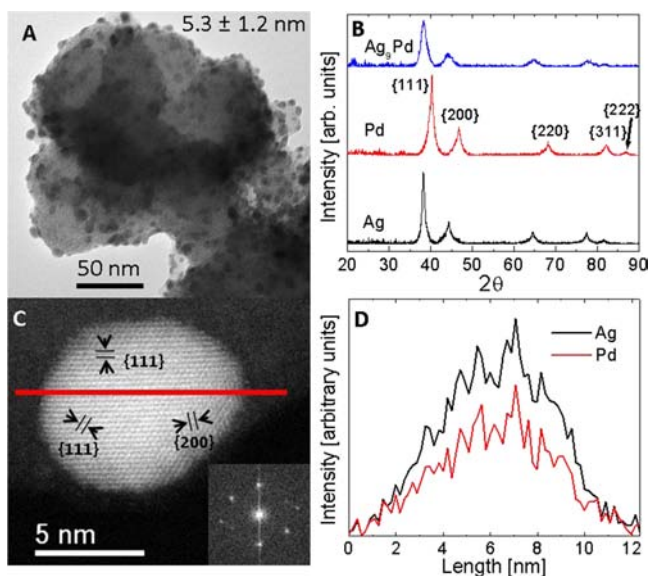


Figure 1. Ag₉Pd nanoparticles supported on Vulcan XC72 carbon after calcination at 350 °C in N₂ as shown by (A) TEM and (B) XRD. The TEM shows that the particles are uniformly distributed over VC with an average particle size of 5.3 ± 1.2 nm. The peak for {111} is located between both pure Pd and Ag due to the alloying with 10 mol % Pd (as confirmed by Vegard's law). The lack of additional peak shoulders suggests that the particles are composed of a single alloy phase, Ag₉Pd. The uniform composition is confirmed by the STEM EDS line scan (C,D). Furthermore, the particles are shown to be composed primarily of {111} facets (C, inset), along with twinning for the {111}.

Table 1. Summary of Catalyst Loading, Morphology, and Composition

catalyst	loading [wt %]	size [nm]	XRD size [nm]	Vegard's law Ag [mol %]	XPS Ag [mol %]
Ag	28	10.1	11.8	100	100
Ag	28	19.0	—	—	100
Ag ₉ Pd	23	5.3	6.0	90	91
Ag ₄ Pd	23	5.1	4.4	78	83
Ag ₂ Pd	24	6.8	3.7	55	65
AgPd ₂	25	6.6	6.8	36	38
Pd	19	5.7	7.7	~0	~0

consequence of the same tetradecanoate complex for each metal.⁴¹ The lack of peak shoulders for the crystalline reflections from XRD suggests a uniform alloy composition among particles (Figures 1B, S3). The alloy composition can be estimated according to Vegard's law^{48,49} for an unstrained alloy. Here, the composition of the alloy follows a simple linear relationship based on the shift in lattice constant of the alloy from that of either of the pure components. The compositions correspond closely to the starting precursor ratios as shown in Table 1. For example, the atomic percentages calculated using Vegard's law for Ag₉Pd and Ag₄Pd are 90% and 78% Ag, respectively. The compositions measured by XPS shown in Figure 2 are in agreement with the less quantitative results calculated from Vegard's law. Furthermore, a probe-corrected STEM-EDS line scan across a single Ag₉Pd alloy nanocrystal (Figure 1C,D) directly shows the uniformity of the alloy throughout the particle. Both Ag and Pd have the same signal ratio from the edge to the center of the particle, indicating little intraparticle segregation of metals. It should be noted that due to the significant overlap of the Pd and Ag EDS spectra, which

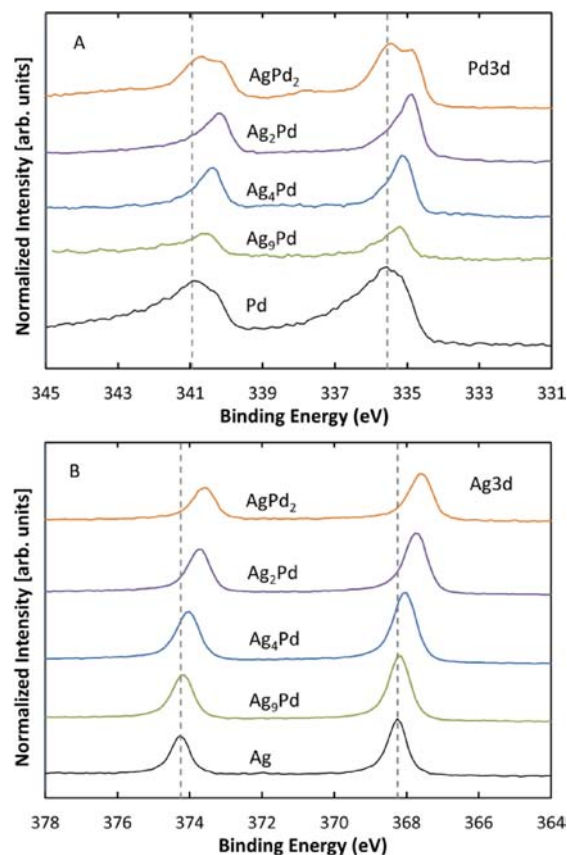


Figure 2. XPS spectra for the (A) Pd3d and (B) Ag3d regions for all Pd:Ag alloy ratios as well as the pure metals. The Pd peaks are shifted negatively for all alloy ratios, as the Pd atoms always have a significant number of Ag atoms with which to interact. However, the Ag peaks only show a shift when the alloy ratio is Ag_{≤4}Pd, when there are enough Pd atoms in the particles to sufficiently disturb the Ag–Ag interactions.

makes deconvolution impractical, this method cannot be used to determine alloy composition quantitatively.

The polarization curves for the most active ORR alloys (Ag₉Pd and Ag₄Pd alloys) are shown along with the pure metal components in Figure 3A. Kinetic current densities are measured at –0.05 V vs NHE from the linear sweep voltammograms and calculated according to the Koutechy–Levich equation. Catalyst loadings on Vulcan XC72 carbon were 22, 24, and 23 wt % for Ag₉Pd, Ag₄Pd, and Ag, respectively, as measured by TGA (Figure S4), comparable to the 20 wt % commercial Pd on Vulcan XC72 for a meaningful comparison of activities. Additional polarization curves and activities are provided in the Supporting Information (Figure S5) and Table 2, indicating a nonlinear enhancement, with the largest activity boost occurring for Ag₉Pd and Ag₄Pd. The synergy in the activity is depicted for all of the catalysts in Figure 3B. Here, all of the activities lie above the line drawn between the pure components. The overall activity of AgPd₂ is actually 60% higher than for Pd. A factor of 3.2 above the linear combination in activities was achieved for Ag₄Pd, as shown in Table 2, suggesting that the presence of both Ag and Pd provides synergistic enhancement. An activity of ~207 mA/mg_{Ag+Pd} would be expected for an alloy with 80 mol % Ag (~60 mA/mg_{Ag}) and 20 mol % Pd (~799 mA/mg_{Pd}), assuming a linear combination of pure component activities. However, the measured activity was ~598 mA/mg_{Ag+Pd} for the Ag₄Pd catalyst,

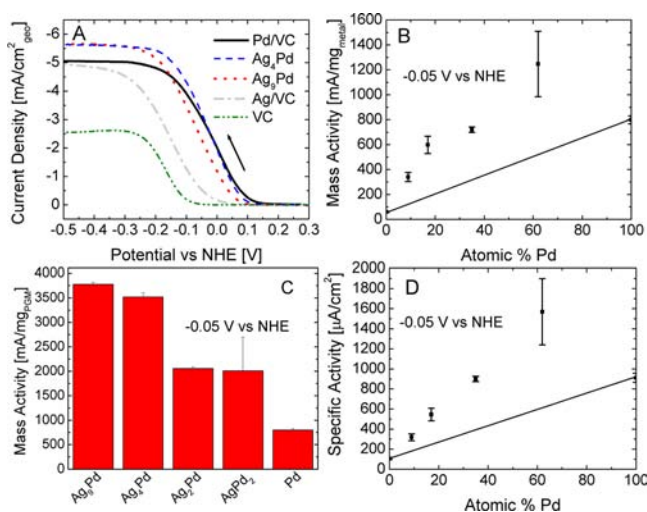


Figure 3. Oxygen reduction activity comparison between Ag-rich alloys and pure components. (A) Linear sweep voltammograms from a rotating disk electrode measurement in O_2 saturated 0.1 M KOH. The diffusion-limited current density for the alloy corresponds to a 4 electron process, higher than either pure Ag or Pd (3.4). (B) Synergy plot of mass activity normalized by total metal loading versus Pd composition. The solid line indicates the linear combination of activities between the pure Ag and Pd components. All of the activities lie above the solid line, indicating a synergy in ORR activities across the compositional range. (C) Bar plot summarizing the ORR activity per Pd loading. The synergy between the Ag and Pd in the alloy achieves a Pd mass normalized activity of 4.7 \times over the commercial Pd/VC and up to 3.2 \times over the linear combination of mass activities for pure Ag and Pd. (D) Synergy plot of specific activity, where the solid line indicates a linear combination of pure component specific activities. Currents were normalized by metal particle surface areas based on measured TEM diameters.

3.2 \times above this prediction. Similar trends are observed for other Ag-rich alloys, including a 2.7-fold increase in Ag_9Pd , whereas for alloy ratios of Ag_2Pd and $AgPd_2$, the enhancement is slightly lower (ca. 2.3 \times). The Pd-based mass activities are summarized in the histograms in Figure 3C and Table 2. By mass of Pd, the alloy is up to 4.7 \times more active than pure Pd, with a value of 3778 mA/mg_{Pd} for Ag_9Pd versus 799 mA/mg_{Pd} for pure Pd/VC. On the basis of the size of the nanoparticles as measured from TEM, an estimated specific activity was calculated and summarized in Table 2 and plotted in Figure 3D. The specific activity increases monotonically with increasing Pd composition, reaching a maximum of 2.6 \times above the expected value for the linear combination of pure metal specific activities. Because of the difference in particle size for pure silver (19 or 10 nm) versus the other catalysts in this

study (~ 5 nm), it may be reasonable to assume that the Ag mass activity could increase if it were ~ 5 nm, due to an increased surface to mass ratio. However, a slower rate of four-electron reduction was observed for 20 nm Ag particles relative to 100 nm particles, which was attributed to fewer of the more active terrace sites on the smaller particles.^{20,50} In our study, we observed specific activities of 106 and 151 mA/cm² for 10 and 19 nm Ag particles, respectively. Therefore, it is unclear that smaller particles of Ag would demonstrate higher activity; however, 10 nm Ag is used for comparison in the synergy plots for both mass and specific activity.

The onset potential for the ORR is ~ 20 mV for Ag as compared to ~ 130 mV for pure Pd (Figure 3A). For the Ag_9Pd alloy, the onset potential is shifted positively ~ 100 mV, despite only 10 mol % Pd incorporated in the Ag. This shift is significantly greater than the potential of 31 mV expected for a linear combination from the pure metals. For the Ag_4Pd alloy, the calculated number of electrons transferred for the ORR, from the Levich equation, based on the diffusion-limited currents was higher than the value of 3.4 observed for both Ag and Pd (Figure 3, Table 2). At a ratio of Ag_9Pd , the electron transfer number reached 4, indicating high efficiency for the full reduction of oxygen.⁵¹ The synergy from alloy Ag and Pd suggests that ligand and atomic ensemble effects are at play, as we elaborate below.

Cyclic voltammetry (CV) was used to probe the surface composition of the nanoalloys (Figures 4 and S7). The CV for

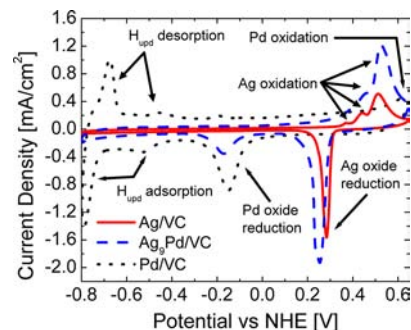


Figure 4. Cyclic voltammograms showing the characteristic redox peaks for the alloy and pure metal catalysts supported on Vulcan XC72 carbon. The presence of both Ag and Pd oxide reduction peaks shows that the surface is composed of both metals. However, the lack of H_{upd} for the alloy suggests that the Pd is dispersed primarily as single atomic sites. The silver oxidation peaks from 0.3 to 0.6 V shift slightly positive for the alloy catalyst, suggesting some resistance to oxidation due to the small amount of Pd. The large reduction peak of silver oxide is shifted negative, suggesting slightly more stable oxide formation.

Table 2. Summary of ORR Activity for AgPd Alloy Compositions and Pure Component Benchmarks at -0.05 V vs NHE

catalyst	total mass activity [mA/mg _{total metal}]	synergy factor for total mass activity	PGM mass activity [mA/mg _{Pd}]	specific activity ^a [μ A/cm ²]	synergy factor for specific activity	no. of electrons
Ag(10 nm)	60	1.0	—	106	1.0	3.4
Ag_9Pd	340	2.7	3778	319	1.8	4
Ag_4Pd	598	3.2	3518	546	2.2	3.7
Ag_2Pd	720	2.3	2057	900	2.3	3.6
$AgPd_2$	1247	2.4	2011	1570	2.6	3.7
Pd	799	1.0	799	912	1.0	3.4
VC	0.50	—	—	—	—	1.7

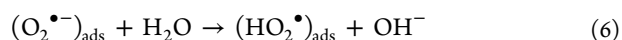
^aSpecific activities normalized by surface areas calculated from TEM diameters.

pure Pd in Figure 4 contains the expected adsorption and desorption of H_{upd} from -0.4 to -0.8 V, along with the characteristic Pd oxide reduction at -0.15 V. In contrast, for the pure Ag catalyst, no features are observed for adsorption and desorption of H^+ characteristic of pure Ag.²⁰ However, when the Ag catalyst is scanned positive of 0.35 V vs NHE, three characteristic oxidation peaks develop at 0.37 , 0.45 , and 0.5 V, corresponding to Ag_2O monolayer formation, $AgOH$ bulk, and Ag_2O bulk, respectively.^{29,43} The reduction of silver oxide is observed to be reversible on the negative scan, at ~ 0.32 V. The CV of the Ag_9Pd alloy catalysts shows oxide reduction peaks for both Pd (-0.17 V) and Ag (0.25 V), indicating that both metals are electroactive at the surface. However, it appears that the location of the metals in the surface has a profound effect on reaction characteristics. At negative potentials, associated with hydrogen adsorption/desorption, the alloy displays no peaks, similar to the response for a pure Ag surface. Previous reports on Pd–Au alloys also demonstrate this behavior, suggesting that a minimum cluster size of Pd dimers is required to show hydrogen adsorption/desorption. Similarly, our results suggest single Pd atoms are dispersed in the Ag-rich surface domains.¹⁴

For alloy ratios $Ag_{\leq 2}Pd$, the H_{upd} peaks, characteristic of pure Pd, emerge, while the ratios of the peak intensities for Pd reduction versus Ag oxidation increase (Figure S6). At these high Pd levels, Pd–Pd contacts in the alloy surface are readily available to processes that depend upon contiguous Pd atoms. CO stripping experiments on the Ag_9Pd alloy (Figure S7) support the evidence from CVs, that both Pd and Ag are present on the surface and that isolated Pd–Pd domains are negligible. Ag shows no peak associated with CO oxidation (stripping),⁵² while Pd shows a sharp CO oxidation peak at ~ 0.1 V. However, the alloy shows only two diffuse peaks at -0.05 and 0.2 V, again indicating an absence of Pd surface clusters with greater than three atoms. In summary, the absence of specific signatures in the CVs for adsorption of both H^+ and the Pd or Ag oxidation/reduction peaks indicates that the Pd is highly dispersed in the surface of the alloy, with minimal binary and higher Pd–Pd domains for $Ag_{\geq 4}Pd$. For all alloy systems, both Pd and Ag are well alloyed and available in the surface of the small nanoalloy particles for the ORR, which is essential for achieving enhanced catalytic activity from ligand and ensemble effects.

Insight into the ligand effect, where the electronic structure of the metals changes due to alloying, can be gleaned from the binding energy shifts in XPS^{1,3} and consideration of the reaction steps for the ORR. The binding energies for both Ag and Pd are shifted negatively (Figure 2, Table S1), consistent with observations for PdAg alloy films.¹⁰ For Ag_9Pd in Figure 2, the peaks for the Pd 3d doublet are shifted by ~ 0.4 eV to lower binding energies, while the Ag is shifted negative by only ~ 0.1 eV (on the order of the instrument resolution). A smaller binding energy (BE) shift is observed for the Ag 3d doublet, as it is in 9-fold excess of the Pd, causing an attenuation of the shifted signal as seen for AgPd alloys containing a dilute amount of Pd.¹⁰ It has been reported that the BE shifts are due to a gain of charge density in the d-band, concomitant with a loss in the sp-band. According to DFT calculations, an upshift in the d-band center can create a stronger bonding with the oxygen, thereby creating more favorable BE for the ORR intermediates to enhance activity.^{23,53,54} It has been well established that the 2 by 2 pathway, which becomes available in

basic media (eq 2), proceeds via a three-step surface-mediated mechanism:⁵⁵



By increasing the d-band charge density, this may facilitate the initial electron transfer step (eq 4). As Ag has a significantly weaker oxygen binding than Pd,⁵³ an upshift in d-band is especially important for the $Ag_{\geq 4}Pd$ catalysts to increase the oxygen binding affinity of the catalysts for facilitating the first electron transfer step. The uniform alloying among particles ensures that the entire catalyst experiences the d-band shift to achieve higher activities. Furthermore, low interaction energy between oxygen and Au has been shown to result from fully filled bonding and antibonding states.⁵⁶ As Ag and Au have similar electronic structures (with the addition of a filled f shell for Au), this may explain why Ag lies on the weak binding side of the volcano plot. However, when Pd was added to the Au, unoccupied oxygen–metal bonding states appear and contribute to strong oxygen binding, similar to the Pd in the Ag surface for the alloys in this study. However, this electronic ligand effect was shown to play a minor role next to the ensemble effects in PdAg films toward CO adsorption and oxidation.^{10,11} Thus, ligand effects alone are not responsible for the observed activity synergy for the AgPd alloys.

The data strongly support the existence of an ensemble effect, whereby a suitable geometric arrangement of Ag next to Pd surface atoms catalyzes ORR. Previous DFT calculations support this idea, as Ag has weak binding and Pd strong binding on a volcano of activity versus binding,⁵³ suggesting a combination of the metals may result in higher activities.^{54,57} The stronger binding of hydroxyl species on Pd versus Ag has been shown to be the cause of hysteresis in polarization curves,²⁰ and is evidenced in our studies by the much larger double layer capacitance for pure Pd relative to Ag (Figure S6). By creating an alloy surface, the Pd atoms may facilitate the initial oxygen binding (e.g., eq 4), whereas the Ag may help to desorb the reaction products such as OH^- , evidenced by the smaller double layer capacitances for the alloys versus Pd/Vc. For Pd in an Au surface, DFT calculations suggest the most likely spot for oxygen adsorption to occur at the Pd sites, where one O atom binds atop and the other is coordinated in a hollow site.⁵⁶ Similarly, the oxygen may bind at the Pd sites, with one O atom “spilling over” onto the Ag site. When a reaction such as eq 6 occurs, the hydroxyl species could easily leave the surface. This could then allow for the final electron transfer on the Pd site back to form the hydroperoxyl anion, followed by chemical disproportionation on the empty adjacent Ag site. In this way, the full four-electron process can be achieved by combining the fast kinetics of Pd for the first two-electron reduction (eq 2) with the rapid disproportionation on Ag (eq 3). Recently, high ORR activity for a Pd-rich alloy film of Pd_3Fe ²⁶ was attributed to the presence of a less active metal, Fe, in the surface to act as a binding center for ORR intermediates, highlighting the importance of ensemble effects. In contrast, in the current work, the AgPd alloy is shown to exhibit a high level of synergy with a dilute amount of the more active metal, Pd, as well as for higher Pd contents. The high fraction of Pd–Ag versus Pd–Pd contacts for the low content Pd alloys would be expected to be highly beneficial for creating strong ligand and

ensemble effects. Given the much higher cost and activity of Pd relative to Ag, this strategy has the potential to be of great practical benefit.

As far as the authors are aware, high catalytic activity and stability for oxygen reduction through ensemble effects with uniform nanoalloys containing extremely low concentrations of a highly active, precious metal has not been reported previously. The high synergy achieved for the presynthesized $\text{Ag}_{\geq 4}\text{Pd}$ uniform alloy morphology is in contrast to previous reports for Ag catalysts alloyed with a small amount of Pd or Pt, which have shown little to negative synergy in ORR activities.^{30,31,33,34} These AgPd nanoparticle alloys were synthesized by the typical approach of adsorption and reduction of metals salts in the presence of the support,^{30,31} which may lead to nonuniform compositions among particles as a result of the different nucleation and growth rates upon reduction of metal ions, as well as the diffusion and adsorption rates of the growing metal particles on the support.⁵⁸ The lack of intimate mixing between Ag and Pd may lead to decreased electronic and ensemble effects. Thus, it is essential to synthesize uniform nanoalloys to take advantage of low precious metal content by dispersing it throughout the surface of the particles to achieve strong ligand and ensemble effects, in our case producing a mass activity synergy factor up to 3.2 beyond the linear combination of Ag and Pd.

This strategy of enhancing catalyst activity by employing ensemble and ligand effects for a precious metal surrounded primarily by a large number of second metal atoms is an approach fundamentally different from that in the case of core-shell nanoparticles.^{5,6,22,24,59,60} For the core-shell morphology, the more active metal is nearly all in the monolayer shell and available for surface reactions. However, the number of unlike metal contacts at the inside of the shell is lower than in the case of a uniform alloy with both metals at the surface. Both core-shell and alloy morphologies have been contrasted for ~40 nm PdAu catalyst for formic acid oxidation.¹³ Because of the presence of both metals in the surface for ensemble effects, the activity for formic acid oxidation was higher on the alloy surface than for the core shell particles, where unlike metal contacts and thus ensemble effects are weaker. Furthermore, for the smaller 5 nm nanocrystals in the current study, it would not be possible to achieve a low Pd content with a Pd monolayer as in the case of the Ag_9Pd alloy. Thus, the nanoalloy approach is a highly complementary alternative to core-shell catalysts to achieve synergistic effects in catalysis.

CONCLUSIONS

A synthetic strategy has been demonstrated to produce uniform ~5 nm AgPd alloy nanoparticles across a wide compositional range via arrested growth during the simultaneous thermolysis of metal precursors to gain fundamental insight into catalytic mechanisms. The compositions of the particles were tuned to control the fraction of the Pd–Pd versus Ag–Pd contacts on the surface. For alloys of $\text{Ag}_{\geq 4}\text{Pd}$, the surface contained single Pd atoms surrounded by Ag atoms, which maximized the ability of a heteroatomic site to amplify the activity of each Pd atom. Determination of atomic ensembles in the surface was accomplished with cyclic voltammetry and CO stripping, electrochemical techniques sensitive to the local environment of atoms in the surface. This level of atomic information is typically not available for the dominant nanoscale characterization techniques (TEM or STEM). In addition to the geometric structure of the surface, the electronic structure of

the alloy was shown to shift according to XPS, contributing to enhance ORR activities. While synergy in activity was present for all alloy ratios, it reached as much as 3.2 for Ag_4Pd relative to the linear combination of the pure components, and the Pd normalized mass activity was as much as 4.7 times that of pure Pd. Furthermore, the overall mass activity per total metal was 60% higher for AgPd_2 , which equates to a reduction in cost (\$/A) by a factor of 2.3. For low Pd content alloys, the synergy in activity was favored by the high degree Pd–Ag versus Pd–Pd contacts, which modified the Pd electronic structure, and by ensemble effects, evidenced by CV and CO stripping measurements that show the involvement of distinct mechanistic steps the Ag and Pd domains in the alloys. The synergy factor for $\text{Ag}_{\leq 2}\text{Pd}$ may result from ensemble effects from larger domains of Pd surrounded by Ag. These studies provide a general approach for understanding and achieving high synergy in catalyst activity via electronic and ensemble effects.

ASSOCIATED CONTENT

Supporting Information

TEM, cyclic voltammograms, linear sweep voltammograms, XRD, and XPS of other alloy ratios and pure metal standards, as well as CO stripping for Pd, Ag, and Ag_9Pd . This material is available free of charge via the Internet at <http://pubs.acs.org>.

AUTHOR INFORMATION

Corresponding Author

kpj@che.utexas.edu; stevenson@cm.utexas.edu

Notes

The authors declare no competing financial interest.

ACKNOWLEDGMENTS

Financial support of this work was provided by the R.A. Welch Foundation (Grants F-1529, F-1319, and AX-1615) and NSF PREM Grant no. DMR 0934218. We also acknowledge Professor Miguel Jose Yacaman and Dr. Arturo Ponce-Pedraza with their help with the pcSTEM, and the RCMI Center for Interdisciplinary Health Research CIHR. The project described was supported by Award Number 2G12RR013646-11 from the National Center for Research Resources. The Kratos XPS was funded by the National Science Foundation under grant CHE-0618242.

REFERENCES

- (1) Liu, P.; Norskov, J. K. *Phys. Chem. Chem. Phys.* **2001**, *3*, 3814.
- (2) Mavrikakis, M.; Hammer, B.; Norskov, J. K. *Phys. Rev. Lett.* **1998**, *81*, 2819.
- (3) Rodriguez, J. A. *Heterog. Chem. Rev.* **1996**, *3*, 17.
- (4) Fernandez, J. L.; Raghuvver, V.; Manthiram, A.; Bard, A. J. *J. Am. Chem. Soc.* **2005**, *127*, 13100.
- (5) Koh, S.; Strasser, P. *J. Am. Chem. Soc.* **2007**, *129*, 12624.
- (6) Sasaki, K.; Naohara, H.; Cai, Y.; Choi, Y. M.; Liu, P.; Vukmirovic, M. B.; Wang, J. X.; Adzic, R. R. *Angew. Chem., Int. Ed.* **2010**, *49*, 8602.
- (7) Stamenkovic, V. R.; Fowler, B.; Mun, B. S.; Wang, G.; Ross, P. N.; Lucas, C. A.; Markovic, N. M. *Science* **2007**, *315*, 493.
- (8) Chen, M.; Kumar, D.; Yi, C.-W.; Goodman, D. W. *Science* **2005**, *310*, 291.
- (9) Han, P.; Axnanda, S.; Lyubinetsky, I.; Goodman, D. W. *J. Am. Chem. Soc.* **2007**, *129*, 14355.
- (10) Ma, Y.; Bansmann, J.; Diemant, T.; Behm, R. J. *Surf. Sci.* **2009**, *603*, 1046.
- (11) Ma, Y.; Diemant, T.; Bansmann, J.; Behm, R. J. *Phys. Chem. Chem. Phys.* **2011**, *13*, 10741.
- (12) Cuesta, A. *ChemPhysChem* **2011**, *12*, 2375.

- (13) Hong, J. W.; Kim, D.; Lee, Y. W.; Kim, M.; Kang, S. W.; Han, S. *W. Angew. Chem., Int. Ed.* **2011**, *50*, 8876.
- (14) Maroun, F.; Ozanam, F.; Magnussen, O. M.; Behm, R. J. *Science* **2001**, *293*, 1811.
- (15) Bruce, P. G.; Scrosati, B.; Tarascon, J.-M. *Angew. Chem., Int. Ed.* **2008**, *47*, 2930.
- (16) Girishkumar, G.; McCloskey, B.; Luntz, A. C.; Swanson, S.; Wilcke, W. J. *Phys. Chem. Lett.* **2010**, *1*, 2193.
- (17) Han, J. J.; Li, N.; Zhang, T. Y. *J. Power Sources* **2009**, *193*, 885.
- (18) Lu, Y.-C.; Xu, Z.; Gasteiger, H. A.; Chen, S.; Hamad-Schifferli, K.; Shao-Horn, Y. *J. Am. Chem. Soc.* **2010**, *132*, 12170.
- (19) Ogasawara, T.; Debart, A.; Holzapfel, M.; Novak, P.; Bruce, P. G. *J. Am. Chem. Soc.* **2006**, *128*, 1390.
- (20) Spindelov, J. S.; Wieckowski, A. *Phys. Chem. Chem. Phys.* **2007**, *9*, 2654.
- (21) Wiberg, G. K. H.; Mayrhofer, K. J. J.; Arenz, M. *ECS Trans.* **2009**, *19*, 37.
- (22) Adzic, R. R.; Zhang, J.; Sasaki, K.; Vukmirovic, M. B.; Shao, M.; Wang, J. X.; Nilekar, A. U.; Mavrikakis, M.; Valerio, J. A.; Uribe, F. *Top. Catal.* **2007**, *46*, 249.
- (23) Nilekar, A. U.; Xu, Y.; Zhang, J. L.; Vukmirovic, M. B.; Sasaki, K.; Adzic, R. R.; Mavrikakis, M. *Top. Catal.* **2007**, *46*, 276.
- (24) Shao, M. H.; Huang, T.; Liu, P.; Zhang, J.; Sasaki, K.; Vukmirovic, M. B.; Adzic, R. R. *Langmuir* **2006**, *22*, 10409.
- (25) Lima, F. H. B.; Zhang, J.; Shao, M. H.; Sasaki, K.; Vukmirovic, M. B.; Ticianelli, E. A.; Adzic, R. R. *J. Solid State Electrochem.* **2008**, *12*, 399.
- (26) Yang, X.; Hu, J.; Fu, J.; Wu, R.; Koel, B. E. *Angew. Chem., Int. Ed.* **2011**, *50*, 10182.
- (27) Kinoshita, K. *Carbon: Electrochemical and Physicochemical Properties*; John Wiley and Sons: New York, 1988.
- (28) Blizanac, B. B.; Ross, P. N.; Markovic, N. M. *J. Phys. Chem. B* **2006**, *110*, 4735.
- (29) Guo, J.; Hsu, A.; Chu, D.; Chen, R. *J. Phys. Chem. C* **2010**, *114*, 4324.
- (30) Lee, C.-L.; Chiou, H.-P.; Chang, K.-C.; Huang, C.-H. *Int. J. Hydrogen Energy* **2011**, *36*, 2759.
- (31) Martinez-Casillas, D. C.; Vazquez-Huerta, G.; Perez-Robles, J. F.; Solorza-Feria, O. *J. New Mater. Electrochem. Syst.* **2010**, *13*, 163.
- (32) Oliveira, M. C.; Rego, R.; Fernandes, L. S.; Tavares, P. B. *J. Power Sources* **2011**, *196*, 6092.
- (33) Chatenet, M.; Aurousseau, M.; Durand, R.; Andolfatto, F. *J. Electrochem. Soc.* **2003**, *150*, D47.
- (34) Lima, F. H. B.; Sanches, C. D.; Ticianelli, E. A. *J. Electrochem. Soc.* **2005**, *152*, A1466.
- (35) Chen, W.; Kim, J.; Sun, S.; Chen, S. *J. Phys. Chem. C* **2008**, *112*, 3891.
- (36) Gupta, G.; Slanac, D. A.; Kumar, P.; Wiggins-Camacho, J. D.; Wang, X.; Swinnea, S.; More, K. L.; Dai, S.; Stevenson, K. J.; Johnston, K. P. *Chem. Mater.* **2009**, *21*, 4515.
- (37) Slanac, D. A.; Li, L.; Stevenson, K. J.; Johnston, K. *ECS Trans.* **2010**, *33*, 161.
- (38) Xiong, L. F.; Manthiram, A. *J. Mater. Chem.* **2004**, *14*, 1454.
- (39) Zhang, X.; Chan, K. Y. *Chem. Mater.* **2003**, *15*, 451.
- (40) Myers, S. V.; Frenkel, A. I.; Crooks, R. M. *Chem. Mater.* **2009**, *21*, 4824.
- (41) Yamamoto, M.; Kakiuchi, H.; Kashiwagi, Y.; Yoshida, Y.; Ohno, T.; Nakamoto, M. *Bull. Chem. Soc. Jpn.* **2010**, *83*, 1386.
- (42) Abe, K.; Hanada, T.; Yoshida, Y.; Tanigaki, N.; Takiguchi, H.; Nagasawa, H.; Nakamoto, M.; Yamaguchi, T.; Yase, K. *Thin Solid Films* **1998**, *327*, 524.
- (43) Hepel, M.; Tomkiewicz, M. *J. Electrochem. Soc.* **1984**, *131*, 1288.
- (44) Grden, M.; Lukaszewski, M.; Jerkiewicz, G.; Czerwinski, A. *Electrochim. Acta* **2008**, *53*, 7583.
- (45) Gupta, G.; Patel, M. N.; Ferrer, D.; Heitsch, A. T.; Korgel, B. A.; Johnston, K. P. *Chem. Mater.* **2008**, *20*, 5005.
- (46) Luo, W.; Hu, W.; Xiao, S. *J. Phys. Chem. C* **2008**, *112*, 2359.
- (47) Wiley, B.; Sun, Y. G.; Mayers, B.; Xia, Y. N. *Chem.-Eur. J.* **2005**, *11*, 454.
- (48) Vegard, L. Z. *Phys.* **1921**, *5*, 17.
- (49) Vegard, L. Z. *Phys.* **1921**, *5*, 393.
- (50) Yang, Y.; Zhou, Y. *J. Electroanal. Chem.* **1995**, *397*, 271.
- (51) Bidault, F.; Brett, D. J. L.; Middleton, P. H.; Brandon, N. P. *J. Power Sources* **2009**, *187*, 39.
- (52) Nguyen, S. T.; Law, H. M.; Nguyen, H. T.; Kristian, N.; Wang, S.; Chan, S. H.; Wang, X. *Appl. Catal., B* **2009**, *91*, S07.
- (53) Lima, F. H. B.; Zhang, J.; Shao, M. H.; Sasaki, K.; Vukmirovic, M. B.; Ticianelli, E. A.; Adzic, R. R. *J. Phys. Chem. C* **2007**, *111*, 404.
- (54) Norskov, J. K.; Rossmeisl, J.; Logadottir, A.; Lindqvist, L.; Kitchin, J. R.; Bligaard, T.; Jonsson, H. *J. Phys. Chem. B* **2004**, *108*, 17886.
- (55) Wiggins-Camacho, J. D.; Stevenson, K. J. *J. Phys. Chem. C* **2011**, *115*, 20002.
- (56) Dhoubi, A.; Guesmi, H. *Chem. Phys. Lett.* **2012**, *521*, 98.
- (57) Fernandez, J. L.; Walsh, D. A.; Bard, A. J. *J. Am. Chem. Soc.* **2005**, *127*, 357.
- (58) Antolini, E. *Mater. Chem. Phys.* **2003**, *78*, 563.
- (59) Jiang, L.; Hsu, A.; Chu, D.; Chen, R. *Electrochim. Acta* **2010**, *55*, 4506.
- (60) Strasser, P.; Koh, S.; Anniyev, T.; Greeley, J.; More, K.; Yu, C. F.; Liu, Z. C.; Kaya, S.; Nordlund, D.; Ogasawara, H.; Toney, M. F.; Nilsson, A. *Nat. Chem.* **2010**, *2*, 454.